Multi-Island Genetic-Algorithm-Based Approach to Uniquely Calibrate Polycrystal Plasticity Models for Magnesium Alloys

XIAOCHUAN SUN,[1,2] BO ZHANG,[3,6] YAODONG JIANG,[4] PEIDONG WU,[5] and HUAMIAO WANG [1,2,7]

1.—State Key Laboratory of Mechanical System and Vibration, Shanghai Jiao Tong University, Shanghai 200240, China. 2.—Materials Genome Initiative Center, Shanghai Jiao Tong University, Shanghai 200240, China. 3.—State Key Laboratory of Hydroscience and Engineering, Tsinghua University, Beijing 100084, China. 4.—School of Mechanics & Civil Engineering, China University of Mining and Technology (Beijing), Beijing 100083, China. 5.—Department of Mechanical Engineering, McMaster University, Hamilton, Ontario L8S 4L7, Canada. 6.—e-mail: zbdth@mail.tsinghua.edu.cn. 7.—e-mail: wanghm02@sjtu.edu.cn

The single-crystal yielding and hardening behavior of polycrystals is important for understanding their mechanical behavior. Many parameters (> 10) are usually required to achieve this for magnesium alloys based on physics-based models. However, the efficient and precise determination of these parameters is a very challenging task. An efficient and practical method is proposed herein to determine the parameter set by dividing the parameters into those for yielding and hardening, thereby significantly reducing the time cost of automatic parameter calibration. This method is then applied to calibrate the parameter set used in the viscoplastic self-consistent (VPSC) model to describe the mechanical behavior of the rare-earth magnesium alloy ZEK100 from multiple mechanical test data. The obtained best-fit parameters can be considered realistic and nearly unique, and can successfully reproduce the mechanical behavior and textural evolution. This procedure can be generally applied to calibrate near-unique parameters in other materials and constitutive models.

INTRODUCTION

In recent years, magnesium (Mg) alloys, as lightweight materials with high specific strength, have attracted much attention from both academia and industry.[1] Because of the hexagonal close-packed (HCP) crystallographic structure of Mg alloys, several concurrent deformation mechanisms, such as slip systems and extension twinning, will be activated differently depending on the loading.[2,3] The less active pyramidal slip system explains the poor room-temperature formability of conventional Mg alloys. However, addition of rare-earth (RE) elements, such as Nd, Ce, Y, and Gd, can overcome this limitation[4–9] by drastically changing their properties.[10]

Carrying out mechanical measurements on single-crystal Mg alloys is a common approach to investigate the effect of RE elements on the deformation mechanism. This can determine the corresponding single-crystal properties describing the mechanical behaviors, e.g., channel die compression tests on pure Mg, Mg-0.5%Th, and Mg-4%Li,[11] micropillar compression measurements of pure Mg and Mg-0.2%Ce,[10,12–15] etc. However, because of the difficulty in growing sufficiently large single crystals and the strong size effect observed for small specimens, direct measurement of single-crystal properties is either unlikely or not applicable for bulk polycrystalline Mg alloys. Given that more data are available on the mechanical response of polycrystalline Mg alloys, an alternative method for determining the single-crystal properties is to fit these polycrystalline data using physics-based

polycrystalline models.[3,16,17] In these crystal plasticity models, a particular set of single-crystal parameters usually represent the single-crystal properties.

However, precise determination of the single-crystal parameters of Mg alloys relies strongly on the twinning model applied. Therefore, the use of an inadequate twinning model can result in an unsatisfactory match between certain experiments and simulations.[17] During the last few decades, various twinning models have been developed.[18–22] Among others, the twinning and detwinning (TDT) scheme exhibits better performance, not only for the macroscopic stress–strain response but also the microscopic internal elastic strain and texture evolution.[22–25] The single-crystal parameters of Mg alloys might be more accurately determined by using the TDT scheme.

Therefore, these single-crystal parameters can be obtained by calibrating the macroscopic mechanical response. The polycrystalline model can then reproduce the relative activity of the deformation mechanisms and the texture evolution, which is difficult to obtain experimentally but can help understand the deformation mechanism of the RE-Mg alloy. However, the determination of a unique set of these parameters is challenging. Due to the multiple deformation mechanisms operating in such materials, which have different hardening properties, the large number of combinations of these parameters makes it very difficult to obtain a unique set of single-crystal parameters.

An often-used approach is to calibrate two mechanical tests: one dominated by twinning and another that is hardly relevant to twinning, such as monotonic tension and compression along the rolling direction (RD) of an Mg alloy sheet and commercial pure Ti grade 1.[16,25] This method can effectively separate the calibration of the twinning parameters from those associated with other deformation mechanisms. However, the uniqueness of the obtained parameters is always questionable, and the calibration of such parameters is still time consuming, even when adopting automatic optimization methods such as the genetic algorithm.[17] An approach that can precisely determine the parameter set is highly desired for understanding and modeling the mechanical behavior of such polycrystals.

In the current work, a practical approach to efficiently calibrate the parameter set of Mg alloy sheets using the multi-island genetic algorithm (MIGA) is proposed and further applied to obtain the parameter set for ZEK100 Mg alloy sheet. The physics-based model employed is the viscoplastic self-consistent model incorporating the TDT scheme (denoted as the VPSC-TDT model). An extended Voce hardening law that has been demonstrated to be able to describe the hardening behavior of Mg alloys is used to demonstrate the efficiency of the proposed approach. The combined effect of the various deformation mechanisms is also discussed in detail.

PROBLEM FORMULATION AND SOLUTION METHOD

Simulation Method

The VPSC-TDT model is only briefly described here. Detailed descriptions can be found elsewhere.[22] The shear rate for both slip and twinning systems is expressed in power-law form as

$$\dot{\gamma} = \dot{\gamma}_0 |\tau/\tau_{cr}|^{\frac{1}{m}} sgn(\tau) \tag{1}$$

where $\dot{\gamma}_0$ is a reference shear rate, τ is the resolved shear stress, τ_{cr} is the critical resolved shear stress (CRSS), and m is the strain rate sensitivity. Equation 1 is valid for twinning only when the RSS is in the right direction, while the shear rate is zero otherwise. The twinned and untwinned portions are the twin and matrix, which are treated as independent grains to interact with the homogeneous effective medium (HEM). The orientation of the twin is updated via the twin–matrix orientation relation. Along with deformation, the twin will evolve through growth (twinning) or shrinkage (detwinning), but their summed volume fraction remains the same as in the original grain.

For both slip and twinning, the CRSS is updated as

$$\tau_{cr}^{\alpha} = \frac{d\hat{\tau}^{\alpha}}{d\Gamma} \sum_{\beta} \theta^{\alpha\beta} |\dot{\gamma}^{\beta}| \tag{2}$$

where $\theta^{\alpha\beta}$ are the latent hardening coupling coefficients, which empirically account for the obstacles to deformation system α associated with system β. $\hat{\tau}^{\alpha}$ is the threshold stress and is given in Eq. 1. Its evolution with the accumulated shear strain is described by an extended Voce hardening law of the form[26]

$$\hat{\tau}^{\alpha} = \tau_0^{\alpha} + (\tau_1^{\alpha} + h_1^{\alpha}\Gamma)\left(1 - \exp\left(-\frac{h_0^{\alpha}}{\tau_1^{\alpha}}\Gamma\right)\right) \tag{3}$$

where $\Gamma = \sum_{\alpha} \int |\dot{\gamma}^{\alpha}| dt$ is the accumulated shear strain, τ_0 and $\tau_0 + \tau_1$ are the initial and back-extrapolated CRSSs, and h_0 and h_1 are the initial and asymptotic hardening rates, respectively. Apparently, only four parameters need to be determined $(\tau_0^{\alpha}, \tau_1^{\alpha}, h_0^{\alpha}, h_1^{\alpha})$ to accurately reproduce the CRSS evolution for an explicit deformation system α, making the Voce law a practical model that is widely adopted in most such works.[17,27–29]

The threshold volume fraction V^{th} used to turn-off twinning is defined as

$$V^{th} = \min\left(1.0, A_1 + A_2 \frac{V^{eff}}{V^{acc}}\right) \tag{4}$$

where A_1 and A_2 are two material constants. The two statistical variables V^{acc} and V^{eff} are the weighted volume fraction of the twinned region and the volume fraction of twin-terminated grains, respectively. According to Eq. 4, the minimum twin volume fraction (TVF) allowed among the grains is A_1, while the maximum TVF allowed is not a constant but depends on the twinning history.

Procedure for Calibrating the Model Parameters

ZEK100 magnesium alloy sheet (1.3%Zn, 0.2%Nd, 0.25%Zr, and 0.01% Mn) is the investigated object. A servohydraulic tensile tester (Instron 1331) was used in the quasistatic tension and compression experiments. Mechanical tests were conducted along four orientations, namely the RD, 45° with respect to the RD (45), the transverse direction (TD), and the normal direction (ND), at a strain rate of 0.001 s^{-1}. The sample size and specific test procedure are referred to Kurukuri et al.[30]

Here, seven experimental datasets for ZEK100 sheet, viz. compression along the RD (C-RD), the transverse direction (C-TD), 45° with respect to RD (C-45), and the normal direction (C-ND), as well as tension along the RD (T-RD), the TD (T-TD), and 45° with respect to RD (T-45),[30] are used to determine the parameters as uniquely as possible. To evaluate the consistency between the experimental data and corresponding simulation results, the respective R^2 values are calculated as

$$R^2 = 1 - \frac{\sum_i \left(\sigma_i^{sim} - \sigma_i^{exp}\right)^2}{\sum_i \left(\sigma_i^{sim} - \overline{\sigma^{sim}}\right)^2} \quad (5)$$

where σ_i^{sim} and σ_i^{exp} represent the simulated and experimental stresses at a plastic strain, and $\overline{\sigma^{sim}}$ is the average of the simulated stresses. Previous work suggests that a reasonable calibration is obtained once R^2 is greater than 0.93. Of course, the higher the R^2 value, the better the calibration.

The main concurrent deformation mechanisms in ZEK100 considered in the VPSC-TDT model are basal slip, prismatic slip, pyramidal slip, and extension twin. Four parameters associated with the Voce hardening law for each system must be calibrated. Among these parameters, h_1, which matters at relatively large deformation, is set to zero for all the deformation mechanisms. In addition, a plateau in the stress–strain curves of Mg alloys associated with twinning indicates that the hardening of extension twins is negligible. Therefore, τ_1, h_0, and h_1 for the extension twin are assumed to be zero. The above considerations reduce the number of parameters to be calibrated from 16 to 10.

MIGA is adopted to find the global optimum in the ten-parameter space. Based on the genetic algorithm, MIGA separates the "population" into several "islands" that are evenly distributed in the whole space. In each generation, the first-class individuals will be selected in all islands while immigration between islands is forbidden, which avoids searching only for local optima. This algorithm has been broadly applied in many optimization works on research and engineering problems recently.[31–33] However, such a ten-dimensional optimization problem requires a large population and evolution for several generations configured in MIGA to guarantee accuracy, which will make the optimization process time-consuming. As the ten parameters have physical meanings, the efficiency of the optimization can be improved by following a "two-stage" procedure:

(1) The range of the yielding and hardening parameters comes from previous related studies about Mg alloys[3,22,24,29,34–37] and listed in Table I.

(2) The hardening parameters are divided into two groups: four yielding parameters $\tau_0^{bas}, \tau_0^{pri}, \tau_0^{pyr}$ and τ_0^{tw} for basal slip, prismatic slip, pyramidal slip, and extension twin, and six hardening parameters $\tau_1^{bas}, \tau_1^{pri}, \tau_1^{pyr}, h_0^{bas}, h_0^{pri}$ and h_0^{pyr} for three slip systems.

(3) The six hardening parameters are randomly selected within the parameter range first. Then, MIGA automatically optimizes the four yielding parameters using the first 2% strain data from the seven experimental case data. The optimization strategy in this step is to find the lowest root-mean-squared error (RMSE) between the simulated and experimental results.

(4) After determining the yielding parameters, the remaining six hardening parameters are calibrated based on the full-range experimental data. The optimization strategy is to maximize the mean R^2 values of all seven cases.

RESULTS AND DISCUSSION

Parameter Calibration

To demonstrate the efficiency of the procedure proposed in "Procedure for Calibrating the Model Parameters" section, direct optimization of all ten parameters using MIGA was also conducted. Table II lists the parameter configurations of MIGA in the ten-dimensional optimization ("10-d calibration" in short) and two-stage optimization (represented as "4+6-d calibration"). Clearly, in the 4+6-d calibration, the required population, the number of islands,

Table I. Range of material parameters for the Mg alloy sheets

Mode	τ_0(MPa)	τ_1(MPa)	h_0 (MPa)
Basal	5–18	1–17	10–200
Prismatic	80–120	1–30	30–500
Pyramidal	110–140	110–160	1000–3000
Extension twin	25–50	–	–

Table II. List of MIGA parameters for the two optimization problems

Problem	Population size	No. of Islands	No. of generations	Crossover rate	Mutation rate
10-d calibration	50	10	10	1	0.1
4+6-d calibration (yielding parameters)	50	10	10	1	0.1
4+6-d calibration (hardening parameters)	30	6	6	1	0.1
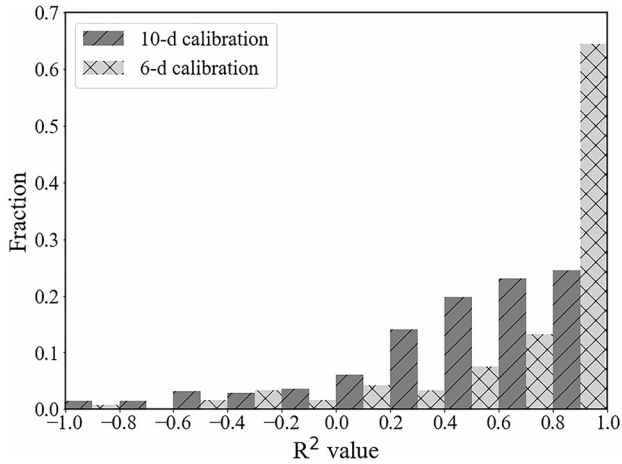
Fig. 1. Distribution of populations' R^2 values in the 10-d and 6-d calibrations.

and the number of generations are significantly decreased.

The high efficiency of the 4+6-d calibration can be attributed to the lower dimension and higher elite rate. The four yielding parameters are determined based on the stress–strain relation in the first 2% strain (step 3), which costs only $\sim$ 10% the time of the 10-d calibration. The other six hardening parameters are then calibrated based on the remaining stress–strain relation, which costs $\sim$ 36% of the time of the 10-d calibration (step 4, also referred to as "6-d calibration"). The dimensional reduction allows the reduction of the required population in the MIGA configuration. Besides, the determination of the four yielding parameters improves the elite rate in the ensuing 6-d calibration. Here, an elite is defined as an "individual" with R^2 value greater than 0.9. Figure 1 shows the distribution of the populations' R^2 values in the 10-d calibration and the 6-d calibration. The elite rate is only 6.7% in the 10-d calibration but reaches 41.3% in the 6-d calibration among all generations. With a significantly higher elite rate, MIGA can find the optimum solution in the 6-d calibration much more quickly, which reduces the number of generations required. The smaller population and fewer generations make the new approach more efficient and

lead to a nearly 54% reduction of the total time consumption.

The 10-d and 4+6-d calibrations do not yield the same optimized results. Table III compares the two optimum sets of parameters. The R^2 value of the 10-d calibration optimum is 0.932, while that of the 6-d calibration optimum is 0.962. The set of parameters obtained from the 4+6-d calibration is the "best fit." This result shows that the new calibration approach can achieve even higher accuracy as well as higher efficiency.

Due to the random search and random mutation of the MIGA, the obtained "global optimum" may not be rigorously optimal locally. To determine whether it is optimal locally, auxiliary simulations were conducted with 10% variation in both the yielding and hardening parameters. The corresponding R^2 values (Table IV) are all smaller than that of the "best-fit" parameters, indicating that the "best-fit" parameters can be regarded as the global optimum.

Texture Evolution

The initial texture of the ZEK100 sheet is presented in Fig. 2, exhibiting a relatively weak basal texture compared with that of commercial Mg alloy AZ31 sheet due to the addition of RE elements. The basal poles are spread in the TD with two prominent peaks, which is an essential characteristic of the grain orientation distribution of ZEK100 sheet. Using the "best-fit" set of parameters (Table III), the VPSC-TDT model predicts the deformation textures under different loading conditions at strains of 10% and 20% (Fig. 2), which is in good agreement with the measured textures.[30]

The texture evolution indicates which deformation mechanisms are mainly activated under different loadings. When basal and prismatic slips are the dominant active deformation mechanisms (e.g., T-RD, T-TD, T-45, and C-ND), the deformation textures show a generally similar characteristic to the initial texture (Fig. 2). The quantitative difference among these deformation textures is ascribed to the relatively different activity of basal slip and prismatic slip. However, when the extension twin is the dominant active deformation mechanism (e.g., C-RD, CTD, C-45, and T-ND), the deformation

Table III. Optimum set of parameters for ZEK100 sheet in the 10-d problem and 4+6-d problem, alongside corresponding values for AZ31B sheet for comparison[29]

Parameter/MPa	τ_0^{bas}	τ_0^{pri}	τ_0^{pyr}	τ_0^{tw}	τ_1^{bas}	τ_1^{pri}	τ_1^{pyr}	h_0^{bas}	h_0^{pri}	h_0^{pyr}
10-d calibration optimum	14	105	124	38	7	11	133	25	362	1236
4+6-d calibration optimum "best-fit"	9	110	125	48	2	11	105	93	412	1790
AZ31B sheet	5	95	105	37	7	30	110	150	350	3000

Table IV. R^2 values of auxiliary simulations with 10% variation of each parameter

Adjusted parameter	τ_0^{bas}	τ_0^{pri}	τ_0^{pyr}	τ_0^{tw}	τ_1^{bas}	τ_1^{pri}	τ_1^{pyr}	h_0^{bas}	h_0^{pri}	h_0^{pyr}
+10%	0.952	0.804	0.933	0.958	0.954	0.956	0.946	0.957	0.956	0.952
−10%	0.954	0.822	0.960	0.955	0.952	0.954	0.958	0.957	0.958	0.960
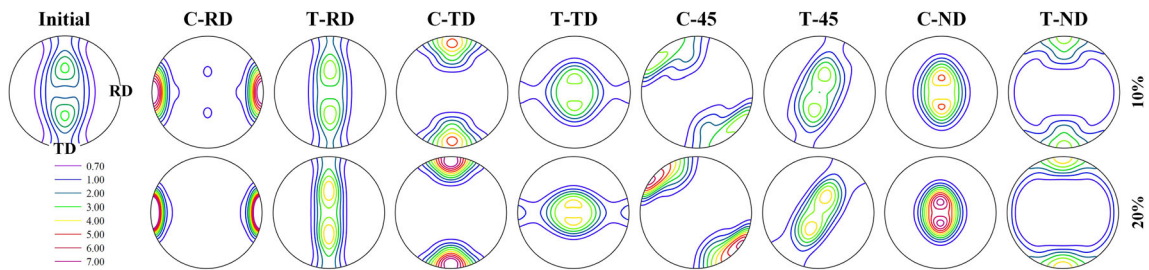
Fig. 2. Initial and developed textures of rolled ZEK100 sheet under different loadings in terms of {0001} pole figures at strain of 10% (top) and 20% (bottom).

textures are drastically different from the initial texture, with the basal poles nearly perpendicular to the initial basal poles. This phenomenon is due to the 86.3° rotation of the grain orientation by extension twin. The different basal pole intensity results from the relatively different contribution of the extension twin (see the twin volume fraction (TVF) in the loading cases).

Mechanical Behavior

According to Table III, the "best-fit" single-crystal parameters for the ZEK100 sheet are quite different from those for the conventional Mg alloy AZ31B[29] (Table III, last row). The ratios between the CRSSs of the nonbasal and basal slips of the ZEK100 sheet are significantly reduced, consistent with the corresponding experimental observations. Relatively, the nonbasal slip modes become easier to be activated, thereby improving the formability of Mg alloys with addition of rare-earth elements.

Based on the "best-fit" parameters, the simulated stress–strain curves (lines in figures) under both tension and compression along the RD (T-RD and C-RD) agree well with experiment (Fig. 3a). The relative activities of the deformation mechanisms

of slips and twinning are presented in Fig. 3b, c. In the C-RD case, with increasing strain, basal slip becomes more active with continuously declining twinning activity. Pyramidal slip is activated with a relatively small fraction at plastic strain beyond 6% (Fig. 3b). As the CRSS values of basal slip and extension twin are relatively low (Table III), the stress under C-RD initiates at a low value of $\sim$ 150MPa and ends up to $\sim$ 450 MPa because of the participation of prismatic slip and pyramidal slip. In the T-RD case, nearly equivalent fractions of deformation are sustained by the basal and prismatic slip, resulting in a high initial yielding stress ($\sim$ 220 MPa) but ending up at only $\sim$ 270 MPa.

Figure 4 presents the stress–strain curves and relative activity of various deformation mechanisms under compression and tension along TD (C-TD and T-TD). The relative activities indicate that, under C-TD, basal slip and extension twin accommodate the plastic deformation in the initial deformation phase with a certain amount of prismatic and pyramidal slip providing further plastic deformation, but the corresponding activities are lower than that of C-RD (Fig. 4b). Meanwhile, under T-TD, the extension twin is noticeable at small strains, which is different
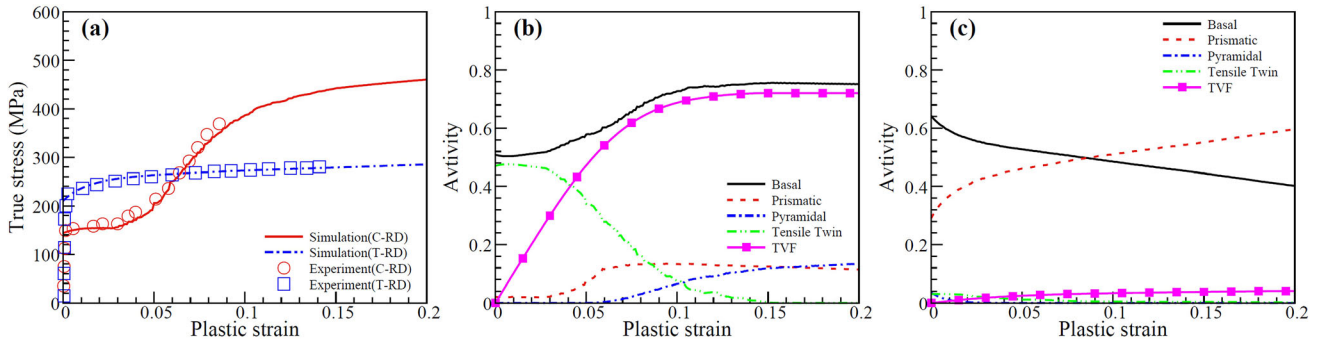
Fig. 3. (a) Stress–strain curves under C-RD and T-RD, and relative activities of various deformation mechanisms under (b) C-RD and (c) T-RD.
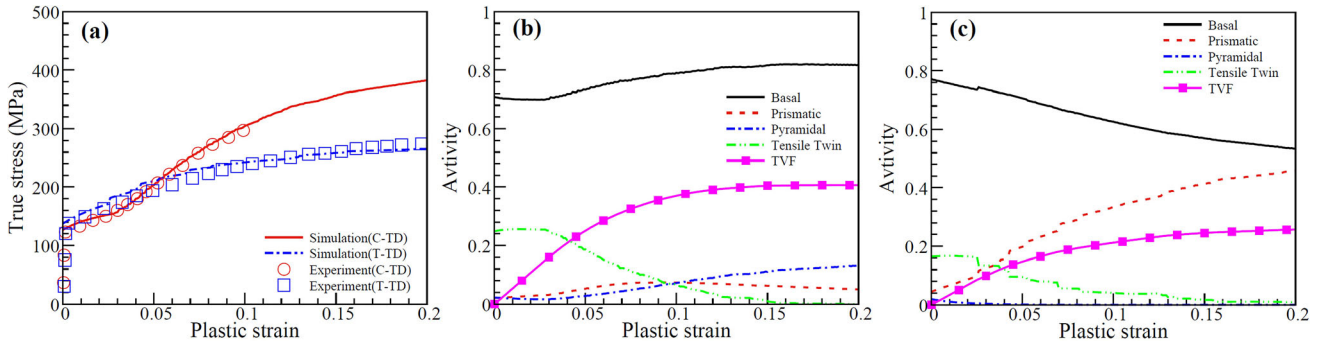

Fig. 4. (a) Stress–strain curves under C-TD and T-TD, and relative activities of various deformation mechanisms under (b) C-TD and (c) T-TD.
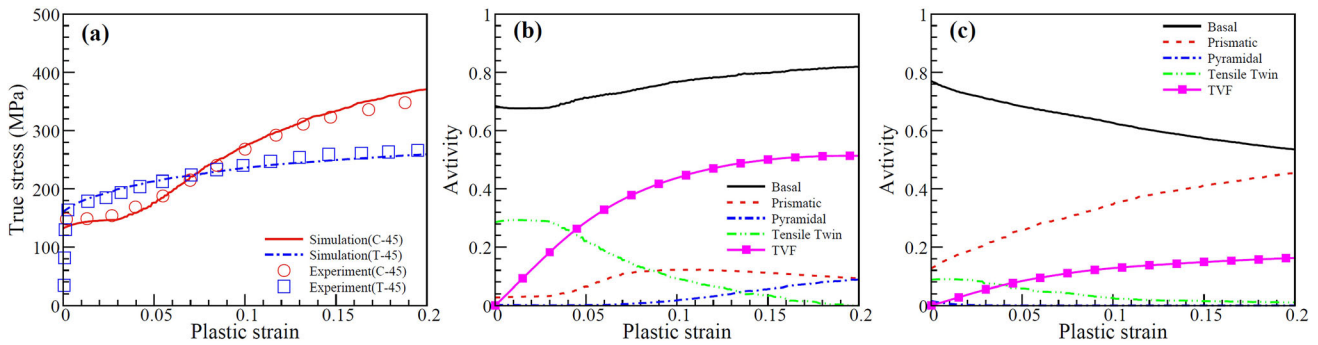

Fig. 5. (a) Stress–strain curves under C-45 and T-45, and relative activities of various deformation mechanisms under (b) C-45 and (c) T-45.

from T-RD, indicating that the mechanism changes from twinning to slip (Fig. 4c).

For loadings of T-45 and C-45 (Fig. 5), the deformation mechanism is similar to C-RD, and pyramidal slip is active after a certain strain. From Fig. 5b, c, it can be seen that the active pyramidal slip is responsible for the rapid hardening of C-45 due to the high CRSS of pyramidal slip. With respect to C-ND (Fig. 6), the plastic deformation is dominated mostly by basal slip and coordinated by prismatic and pyramidal slips, similar to C-TD (Figs. 4b , 6b). Though experimental results are not available, an auxiliary simulation of T-ND (Fig. 6c) was performed. A large amount of twinning coordinate deformation

and prismatic slip becomes more active with the less deformation induced by twin.

According to the results shown in Figs. 3, 4, 5, and 6, the simulated stress–strain curves are consistent with the corresponding experiments. Based on these results, the twinning activity is worth further analysis. The deformation twinning nearly saturates beyond strain of 10% in all the loading cases, after which the slip mechanisms dominate to accommodate the plastic deformation. Besides, higher TVF (more twinning) induces a longer plateau in the stress–strain curves.

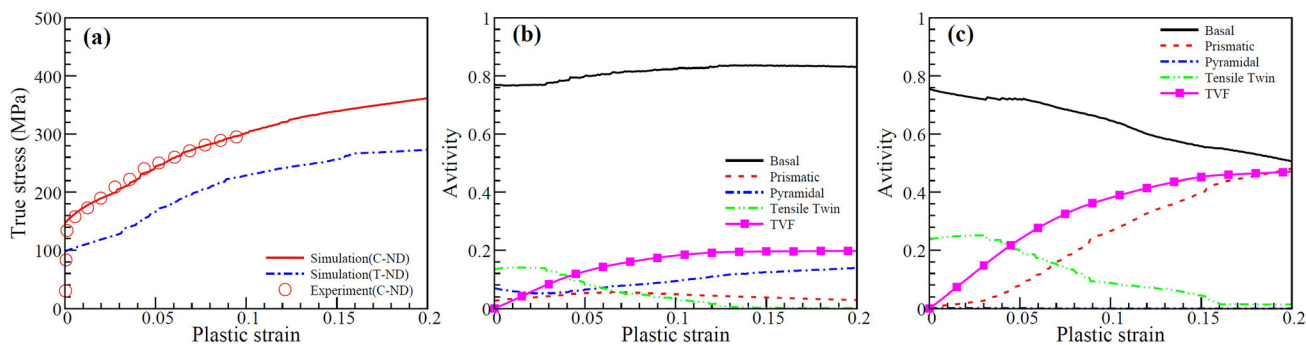In conclusion, the different combinations of the operating deformation mechanisms result in

Fig. 6. (a) Stress–strain curves under C-ND and T-ND, and relative activities of various deformation mechanisms under (b) C-ND and (c) T-ND.

different mechanical responses and texture evolution in the different loading cases.

CONCLUSIONS

A two-stage calibration procedure with MIGA is proposed to calibrate the single-crystal parameters associated with a polycrystal plasticity model (VPSC-TDT model + Voce hardening law here) based on multiple mechanical testing results, exhibiting superior efficiency and accuracy. The new procedure saves $\sim$ 54% of the calibration time of the ten-dimensional calibration. Moreover, the obtained set of parameters is the global optimum.

The optimized set of parameters for ZEK100 alloy reproduces well the strain–stress response, the relative activity of deformation mechanisms, and the texture evolution under seven loadings. The differences between the mechanical responses under different loadings are due to the different deformation mechanisms operating. Principally, the proposed calibration approach does not rely on the constitutive model used and could thus be applied to any other crystal plasticity models or hardening laws.

ACKNOWLEDGEMENT

CONFLICT OF INTEREST

On behalf of all authors, the corresponding author states that there are no conflicts of interest.

REFERENCES

1. T.M. Pollock, T.M. Pollock, *Science* 328, 986. (2010).
2. S.R. Agnew, and Ö. Duygulu, S.R. Agnew, and Ö. Duygulu, *Int. J. Plast.* 21, 1161. (2005).
3. H. Wang, B. Raeisinia, P.D. Wu, S.R. Agnew, and C.N. Tomé, H. Wang, B. Raeisinia, P.D. Wu, S.R. Agnew, and C.N. Tomé, *Int. J. Solids Struct.* 47, 2905. (2010).
4. J. Bohlen, M.R. Nürnberg, J.W. Senn, D. Letzig, and S.R. Agnew, J. Bohlen, M.R. Nürnberg, J.W. Senn, D. Letzig, and S.R. Agnew, *Acta Mater.* 55, 2101. (2007).
5. J. Bohlen, S. Yi, D. Letzig, and K.U. Kainer, J. Bohlen, S. Yi, D. Letzig, and K.U. Kainer, *Mater. Sci. Eng. A* 527, 7092. (2010).
6. K. Hantzsche, J. Bohlen, J. Wendt, K.U. Kainer, S.B. Yi, and D. Letzig, K. Hantzsche, J. Bohlen, J. Wendt, K.U. Kainer, S.B. Yi, and D. Letzig, *Scr. Mater.* 63, 725. (2010).
7. L. Jiang, J.J. Jonas, and R. Mishra, L. Jiang, J.J. Jonas, and R. Mishra, *Mater. Sci. Eng. A* 528, 6596. (2011).
8. C.E. Dreyer, W.V. Chiu, R.H. Wagoner, and S.R. Agnew, C.E. Dreyer, W.V. Chiu, R.H. Wagoner, and S.R. Agnew, *J. Mater. Process. Technol.* 210, 37. (2010).
9. T. Al-Samman, and X. Li, T. Al-Samman, and X. Li, *Mater. Sci. Eng. A* 528, 3809. (2011).
10. J. Ye, R.K. Mishra, A.K. Sachdev, and A.M. Minor, J. Ye, R.K. Mishra, A.K. Sachdev, and A.M. Minor, *Scr. Mater.* 64, 292. (2011).
11. E.W. Kelley, and W. Hosford, E.W. Kelley, and W. Hosford, *Trans Met Soc AIME* 242, 5. (1968).
12. Q. Yu, L. Qi, R.K. Mishra, J. Li, and A.M. Minor, Q. Yu, L. Qi, R.K. Mishra, J. Li, and A.M. Minor, *Proc. Natl. Acad. Sci.* 110, 13289. (2013).
13. C.M. Byer, and K.T. Ramesh, C.M. Byer, and K.T. Ramesh, *Acta Mater.* 61, 3808. (2013).
14. K.E. Prasad, K. Rajesh, and U. Ramamurty, K.E. Prasad, K. Rajesh, and U. Ramamurty, *Acta Mater.* 65, 316. (2014).
15. Y. Liu, N. Li, M. Arul Kumar, S. Pathak, J. Wang, R. J. McCabe, N. A. Mara, and C. N. Tomé, *Acta Mater.* 135, 411 (2017).
16. B. Raeisinia, S. R. Agnew, and A. Akhtar, *Metall. Mater. Trans. A Phys. Metall. Mater. Sci.* 42, 1418 (2011).
17. T. Skippon, C. Mareau, and M.R. Daymond, T. Skippon, C. Mareau, and M.R. Daymond, *J. Appl. Crystallogr.* 45, 627. (2012).
18. P. Van Houtte, P. Van Houtte, *Acta Metall.* 26, 591. (1978).
19. R.A. Lebensohn, and C.N. Tomé, R.A. Lebensohn, and C.N. Tomé, *Acta Metall. Mater.* 41, 2611. (1993).
20. S.R. Kalidindi, S.R. Kalidindi, *J. Mech. Phys. Solids* 46, 267. (1998).
21. G. Proust, C.N. Tomé, and G.C. Kaschner, G. Proust, C.N. Tomé, and G.C. Kaschner, *Acta Mater.* 55, 2137. (2007).
22. H. Wang, P.D. Wu, J. Wang, and C.N. Tomé, H. Wang, P.D. Wu, J. Wang, and C.N. Tomé, *Int. J. Plast.* 49, 36. (2013).
23. H. Qiao, S.R. Agnew, and P.D. Wu, H. Qiao, S.R. Agnew, and P.D. Wu, *Int. J. Plast.* 65, 61. (2015).

24. H. Wang, P. Wu, S. Kurukuri, M.J. Worswick, Y. Peng, D. Tang, and D. Li, H. Wang, P. Wu, S. Kurukuri, M.J. Worswick, Y. Peng, D. Tang, and D. Li, *Int. J. Plast.* 107, 207. (2018).
25. C. Ma, H. Wang, T. Hama, X. Guo, X. Mao, J. Wang, and P. Wu, C. Ma, H. Wang, T. Hama, X. Guo, X. Mao, J. Wang, and P. Wu, *Int. J. Plast.* 121, 261. (2019).
26. C. Tome, G.R. Canova, U.F. Kocks, N. Christodoulou, and J.J. Jonas, C. Tome, G.R. Canova, U.F. Kocks, N. Christodoulou, and J.J. Jonas, *Acta Metall.* 32, 1637. (1984).
27. S.R. Agnew, M.H. Yoo, and C.N. Tomé, S.R. Agnew, M.H. Yoo, and C.N. Tomé, *Acta Mater.* 49, 4277. (2001).
28. H. Wang, P.D. Wu, K.P. Boyle, and K.W. Neale, H. Wang, P.D. Wu, K.P. Boyle, and K.W. Neale, *Int. J. Solids Struct.* 48, 1000. (2011).
29. B. Zhang, S. Li, H. Wang, W. Tang, Y. Jiang, and P. Wu, B. Zhang, S. Li, H. Wang, W. Tang, Y. Jiang, and P. Wu, *Materials (Basel).* 12, 1590. (2019).
30. S. Kurukuri, M. J. Worswick, A. Bardelcik, R. K. Mishra, and J. T. Carter, *Metall. Mater. Trans. A Phys. Metall. Mater. Sci.* 45, 3321 (2014).
31. M.T. Bhoskar, M.O.K. Kulkarni, M.N.K. Kulkarni, M.S.L. Patekar, G.M. Kakandikar, and V.M. Nandedkar, M.T.
Bhoskar, M.O.K. Kulkarni, M.N.K. Kulkarni, M.S.L. Patekar, G.M. Kakandikar, and V.M. Nandedkar, *Mater. Today Proc.* 2, 2624. (2015).
32. T. Liang and H. Lu, *Entropy* 22 (2020).
33. F. Ma, L. Han, Y. Zhou, S. Chen, and Y. Pu, F. Ma, L. Han, Y. Zhou, S. Chen, and Y. Pu, *IEEE Access* 6, 53397. (2018).
34. S.-H. Choi, E.J. Shin, and B.S. Seong, S.-H. Choi, E.J. Shin, and B.S. Seong, *Acta Mater.* 55, 4181. (2007).
35. H. Qiao, X.Q. Guo, A.L. Oppedal, H. El Kadiri, P.D. Wu, and S.R. Agnew, H. Qiao, X.Q. Guo, A.L. Oppedal, H. El Kadiri, P.D. Wu, and S.R. Agnew, *Mater. Sci. Eng. A* 687, 17. (2017).
36. H. Wang, P.D. Wu, C.N. Tomé, and J. Wang, H. Wang, P.D. Wu, C.N. Tomé, and J. Wang, *Int. J. Solids Struct.* 49, 2155. (2012).
37. H. Wang, B. Clausen, C.N. Tomé, and P.D. Wu, H. Wang, B. Clausen, C.N. Tomé, and P.D. Wu, *Acta Mater.* 61, 1179. (2013).